Assiut University Journal of Multidisciplinary Scientific Research (AUNJMSR)
Faculty of Science, Assiut University, Assiut, Egypt.
Printed ISSN 2812-5029
Online ISSN 2812-5037
Vol. 51(2): 200 – 214 (2022)
https://aunj.journals.ekb.eg/

Numerical Site Spectral Amplification Due to Structural Control of Shallow Faults in Wadi Natash, Eastern Desert, Egypt

Mostafa Thabet [1,*]
[1] Geology Department, Faculty of Science, Assiut University
[*]Corresponding Author: e-mail: mostafa.thabet@aun.edu.eg

ARTICLE INFO

Article History:
Received: 15/11/2021
Accepted: 17/4/2022
Online: 1/5/2022

Keywords:
S-wave propagation, guided waves, linear site response, 2D numerical simulation, fault zone

ABSTRACT

Site spectral amplification patterns at Wadi Natash area are exhibited in three frequency band widths of 15 ~ 10 Hz, 10 ~ 7 Hz, and 7 ~ 5 Hz. These amplification patterns result from numerical two-dimensional equivalent linear simulations of propagating *S*-waves at 50 m depth. The *S*-wave's propagation direction is found to be parallel to the dipping direction of the fault plane. Additionally, the resulted amplification patterns above both normal and reverse faults tend to be highly dependent on the frequency band width and fault geometrical parameters. The maximum amplification factors indicate producing very high guided *S*-wave's energy in the overlying fault zone layers. The present results suggest that *S*-wave's guiding efficiency is strongly dependent on the fault type and its relevant parameters, such as fault zone width and fault continuity in layers, and on the frequency band width.

INTRODUCTION

The amplification of earthquake seismic waves could produce increasing seismic damage and consequent significant damage and loss of life. The effect of local site conditions and the relevant impedance contrast of the surficial layers are strongly responsible for producing local amplification during ground motions [1].

Recently, studies by [2] and [3] have focused on analyzing the site effects due to the presence of fault zones. Ground motion amplification of directional effects along a polarized horizontal component could be observed because of active faults and extended fractures (*e.g.* [4]). Directionality effects are observed as variations in horizontal amplifications versus fault zone azimuths ([5], [6], and [7]), indicating anisotropy of *S*-wave velocity (*i.e.* high *S*-wave velocities are parallel to the fault zone, whereas the low

S-wave velocities are normal, causing high amplification). [8] studied ambient seismic noise and concluded that relevant polarization results due to anisotropy in the stiffness related to the complex minor and major faults.

Studying guided *S*-wave's propagation above fault zone structures is important for several reasons. First, since the propagation of guided *S*-waves is affected by the geometry of the fault zone structures, this enables us to find how these fault zone structures could influence the related local site effects. Second, since deep fault zones are thought to consist of regions with reduced seismic velocity, the present research work tries to study shallow fault zones without reduced seismic velocity regions. Moreover, the relationship between the predominant frequency of the propagated input motion and these shallow fault zones has been clarified.

Therefore, the fault zone systems are not considered as low-velocity zones in the present paper. Instead, fault zones that are located in the study area of Wadi Natash are considered as structural dis-continuities of the upper 50 m layers, as interpreted by [9]. Two-dimension (2D) finite element simulations using equivalent linear site response analyses have been carried out along well-defined six 2D profiles. Amplification patterns resulting from these simulations are described at those six 2D profiles to quantify the fault zone-related site responses. Input motions from synthesized sources having various predominant frequencies are used as input motions at 50 m depth. These analyses have important implications for local engineering practice. Therefore, the present investigations exhibit fair comparisons between the amplification response spectra that resulted from various faulted 2D profiles using synthesized input motions with variant predominant frequencies.

GEOLOGIC AND SEISMIC DATA SET

Figure 1 shows the dominant lithology of the study area. Hafafit gneiss domes culmination, which are indicated by A through E letters, are highly affected by normal faults and shear zones along the NW–SE dome margins [10]. Wadi Natash area is covered by recent alluvial fill Wadi deposits. The oldest exposed rocks are mainly Precambrian metavolcanics and cropped out near Wadi Natash area. Turonian sandstones are overlying these exposed rocks. Most of these sedimentary rocks are strongly deformed, which indicates that shearing processes were prevailing during the sedimentation [11].

Figure 2a shows a google location map of the study area. A set of six shallow seismic refraction profiles at the entrance of Wadi Natash area were obtained from a previous research study that was run by [9]. These profiles are extended ENE -WSW

normal to the Red Sea (Figure 2b). The seismic refraction measurements include both the *P*- and *S* -waves velocity structures. The profile spreads have lengths of 550 m with a profile interval of 100 m.

Figure 3 exhibits the present work's interpretation of these six faulted profiles. Three successive lithological units are interpreted. The surficial layer is composed of dry alluvial deposits (sands and gravels) with *P*- and *S*-wave velocities of 600 ~ 1700 m/s and 300 ~ 1000 m/s, respectively. The underlain layer is defined as water-saturated weathered basement rocks with *P*- and *S*-wave velocities of 1700 ~ 4200 m/s and 1300 ~ 2300 m/s, respectively. The massive basement bedrock layer has *P*- and *S*-wave velocities of 4200 ~ 6000 m/s and 2300 ~ 4000 m/s, respectively.

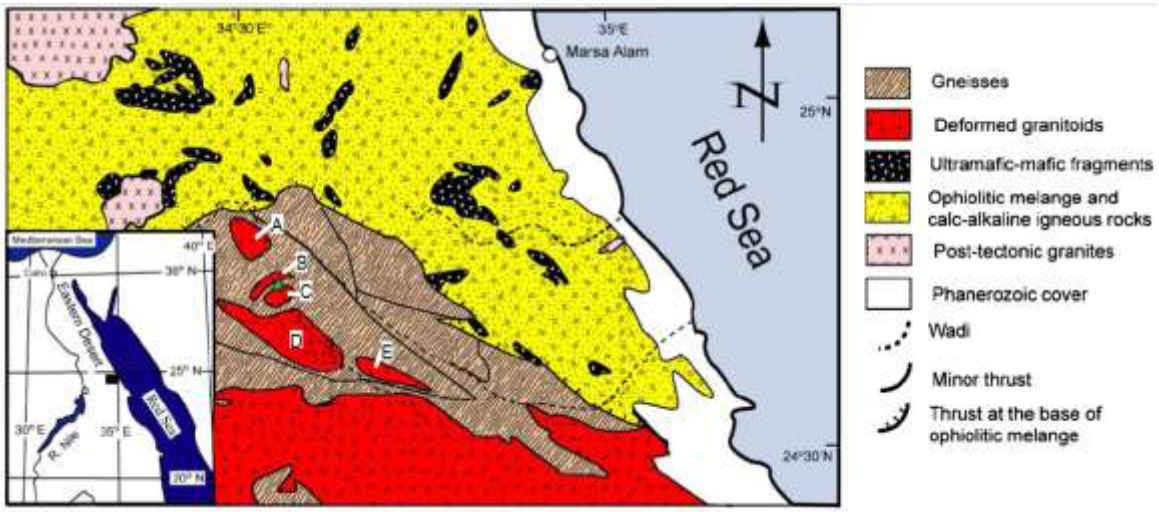

Figure 1. Geological map of the studied area [12]. Green triangle indicates Wadi Natash area.

METHODOLGY

The numerical modeling process consists of the following essential steps:

1. Geotechnical parameters are obtained at each layer for the six profiles. These geotechnical parameters are *P*-wave and *S*-wave velocities, total unit weight, shear modulus at small strains, Poisson's ratio, and damping ratio. The density (ρ) is determined based on [13], as defined in Eq. 1. In this research study, the damping ratio is set to 1% because linear site response is assumed. Table 1 is summarizing the input parameters.

$$\rho = a\, V_P^b \tag{1}$$

where ρ is in g/cm^3, a is 0.31 when V_P is in m/s and is 0.23 when V_P is in ft/s and b is 0.25.

2. Input ground motions are generated at 50 m depth. For this purpose, the stochastic model SMSIM [14] is used to produce synthetic motions due to the absence of recordings in or near the study area. As shown in Table 2, crustal velocity structure of Aswan region (after [15]) is used in synthesizing time histories of the input ground motions at 50 m depth. Five input ground motions are generated with varying predominant frequencies. The time series and their correspondent Fourier spectrum for these generated input ground motions are shown in Figure 4. A Planar wave front is assumed to be incident at 50 m depth. Therefore, at each nodal point at 50 m depth the same input ground motion is propagated using 2D finite element simulations. The maximum acceleration (PGA) of input motions is approximately 2 cm/s^2. This is to ensure conducting linear response analyses throughout the present study.

3. Finite element meshes are created for all the six profiles in the study area in Wadi Natash. Designing the mesh is based upon the concept of an appropriate number of finite elements consistent with the wavelength of the chosen shear wave velocity. As a result, finite elements are basically dependent on the number of nodes and the slowest shear wave velocity throughout the analyzed media. In the present study, the slowest shear wave velocity throughout the entire area of Wadi Natash is 300 m/s, while the highest frequency to be resolved is 20 Hz. This gives a shear wavelength of 15 m. For simple mesh generation, the EasyMesh code program [16] is used. Triangular finite elements are created using Delaunay and constrained Delaunay triangulations.

Table 1: Input parameters for the 2D simulations in the present research work.

	Lithology	**V_p (m/s)**	**V_s (m/s)**	**Density (g/cm^3)**	**Damping ratio**
1st upper layer	Alluvial deposits (sand and gravel)	600 ~ 1700	300 ~ 1000	1.7 ~ 1.9	0.01
2nd middle layer	Water-saturated and fractured basement	1700 ~ 4200	1300 ~ 2300	2.0 ~ 2.6	0.01
3rd lower layer	Massive basement rocks	4200 ~ 6000	2300 ~ 4000	2.6 ~ 3.0	0.01

Table 2: Crustal velocity structure of Aswan region after [15]. (Note that V_p and V_s are *P*- and *S*-wave velocities, respectively)

Depth (km)	**V_p (km/s)**	**V_s (km/s)**
0.00	4.0	2.3
0.50	6.0	3.4
5.00	6.8	3.9
20.0	7.5	4.3

4. Two-dimension finite element simulations are run using the QUAD4M code program [17], which is an equivalent linear two-dimensional code in the time domain. The result from this step is the acceleration time histories at each node of the 2D mesh for each profile.

5. Amplification factors ($A.F.$) are only calculated at each surficial nodal point along the six 2D profiles. The equation of this amplification factor is defined in Eq. 2.

$$A.F. = \frac{S.A._{top}}{S.A._{bottom}} \quad (2)$$

where $S.A._{top}$ is the spectral acceleration at each nodal point at 0 m depth, while $S.A._{bottom}$ is the spectral acceleration at nodal points at 50 m depth.

6. Resulted amplification patterns are discussed and interpreted for each 2D profile.

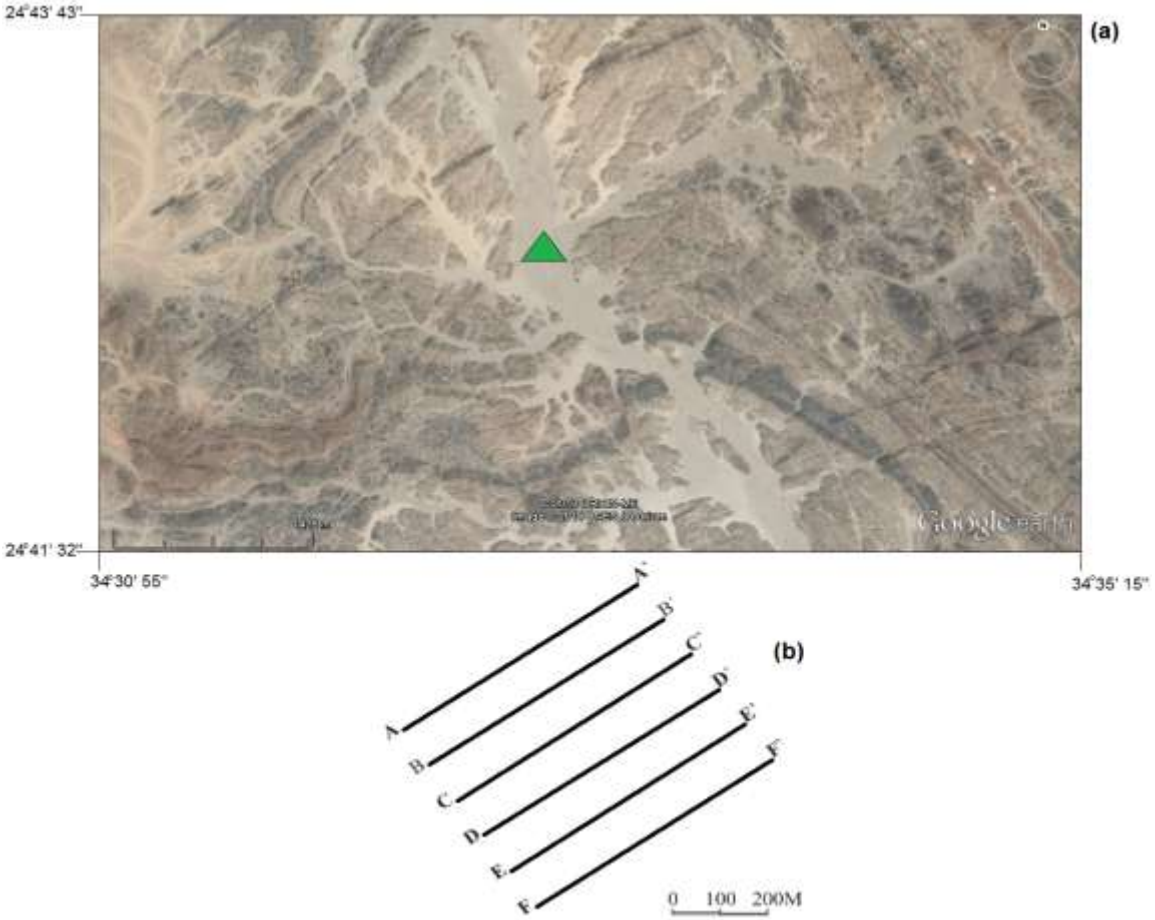

Figure 2. Google Earth map of the study area at Wadi Natash (a), the green triangle is showing the location where of the six shallow seismic refraction profiles with their distribution as shown in (b).

RESULTS AND DISCUSSION

The results of the present research work are shown and discussed in three main categories. These categories depend on the type of faulting in each 2D profile. Profiles AA', BB', and DD' represent normal fault case studies. The normal fault parameters in each profile, such as fault width, fault length and fault dip are different. Profile FF' represents a reverse fault case study. Profiles CC' and EE' represent hybrid normal and reverse fault case studies in Wadi Natash area.

The amplification patterns are shown in three frequency bands as follows: 15 ~ 10 Hz, 10 ~ 7 Hz, and 7 ~ 5 Hz. These frequency band widths are chosen to describe the resultant amplification patterns because of the presence of maximum anomalous behavior of amplification patterns at these frequency band widths.

As shown in Figure 5a, the normal fault in profile AA' extends at a horizontal spread along the ground surface from 250 m to 300 m. The maximum amplification factors exist at the horizontal spread along the ground surface from 0 m to 200 m. Maximum amplification factors are very limited at frequency band widths of 15 ~ 10 Hz and 10 ~ 7 Hz, as shown in Figure 5(b and c), whereas anomalous maximum amplification factors cover a horizontal spread along the ground surface from 100 m to 200 m at a frequency band width of 7 ~ 5 Hz, as shown in Figure 5d.

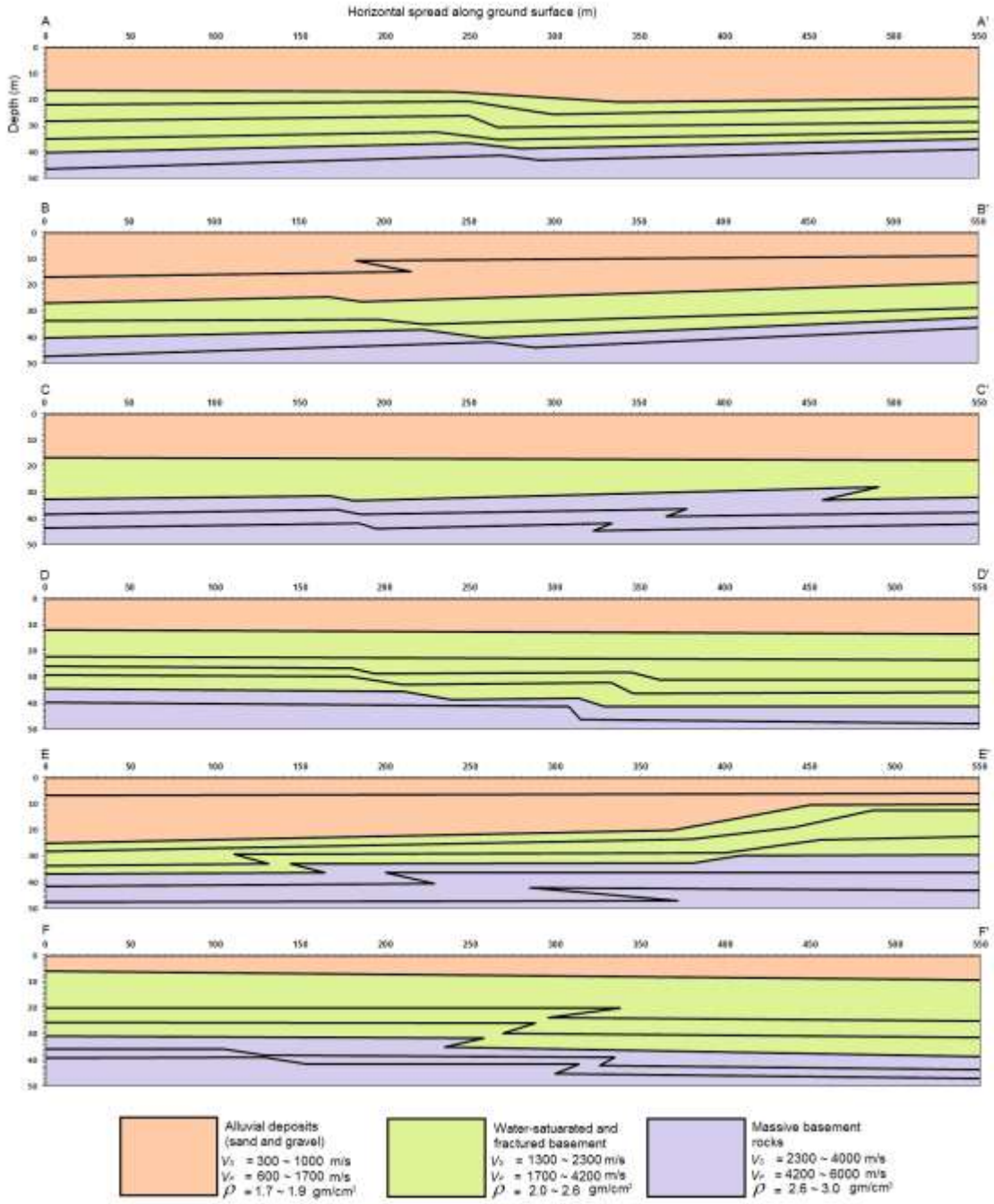

Figure 3. Interpreted six profiles of the shallow *P*- and *S*-wave velocity structures.

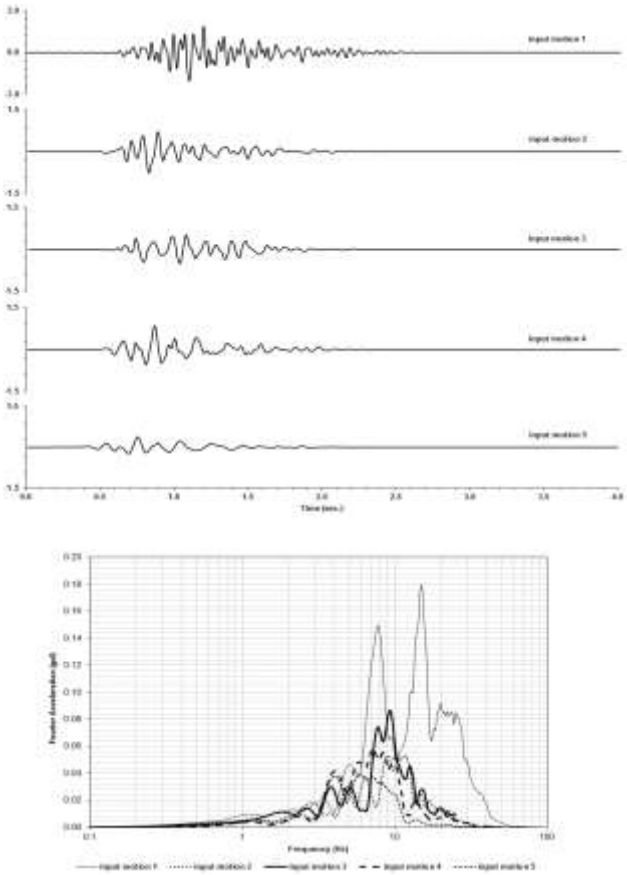

Figure 4. Synthesized input motions that are used in the 2D finite element simulations, time series (upper, note that vertical axis is acceleration in cm/s^2) and their relevant Fourier spectrum (lower).

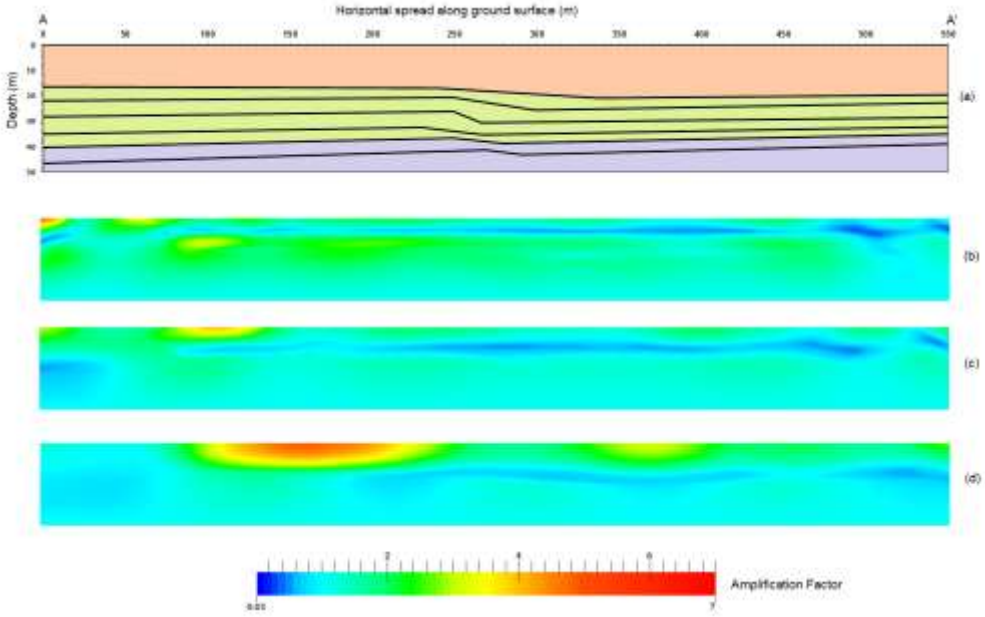

Figure 5. Amplification patterns for profile AA' (a) at frequency bands of 15 ~ 10 Hz (b), 10 ~ 7 Hz (c), and 7 ~ 5 Hz (d).

The normal fault in profile BB' extends at a horizontal spread along the ground surface from 150 m to 300 m, as given in Figure 6a. The amplification patterns at frequency band widths of 15 ~ 10 Hz and 7 ~ 5 Hz are similar to those seen in profile AA', as shown in Figure 6 (b and d). In Figure 6b, the maximum amplification factor is very limited and existed at 15 m depth for a horizontal spread along the ground surface from 50 m to 100 m. Surprisingly, an anomalous maximum amplification factor at a frequency band width of 10 ~ 7 Hz appears at 15 m depth for a horizontal spread along the ground surface between 200 m to 450 m, as shown in Figure 6c. This could be attributed to the presence of trapped energy in the hanging wall side of this normal fault at this frequency band width.

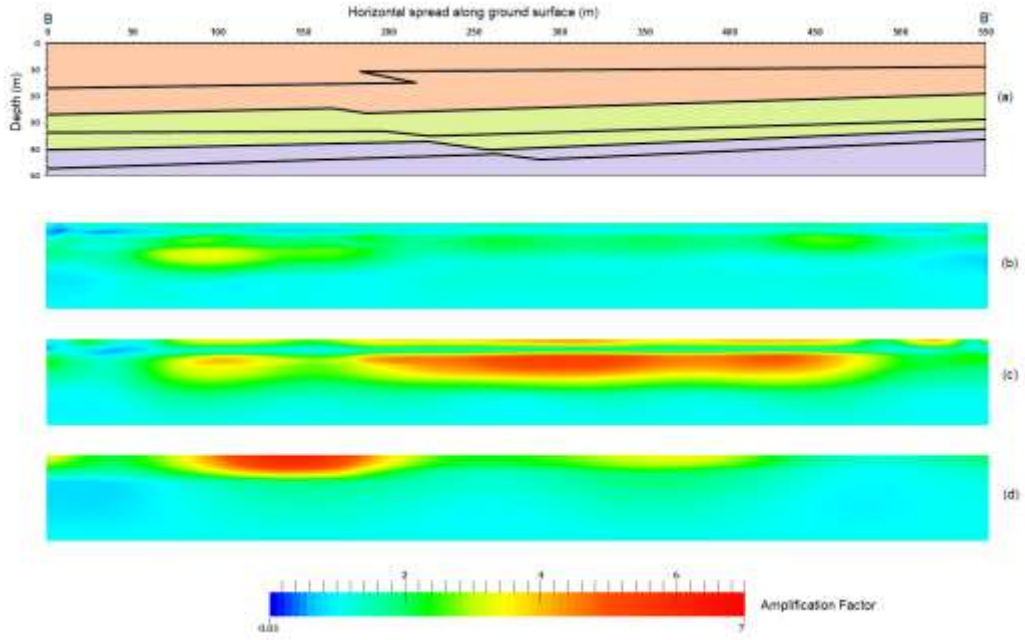

Figure 6. Amplification patterns for profile BB' (a) at frequency bands of 15 ~ 10 Hz (b), 10 ~ 7 Hz (c), and 7 ~ 5 Hz (d).

In profile DD', there are two normal faults (Figure 7a). The first normal fault is dipping toward D' and extends at a horizontal spread along the ground surface from 170 m to 250 m. The second normal fault is dipping toward D and extends at a horizontal spread along the ground surface from 300 m to 350 m. At a frequency band width of 15 ~ 10 Hz, the maximum amplification factors appear at 15 m depths for a horizontal spread along the ground surface from 50 m to 500 m, as shown in Figure 7b. A similar amplification pattern is seen at a frequency band width of 7 ~ 5 Hz, but at depth of 0 m, as given in Figure 6d. At a frequency band width of 10 ~ 7 Hz (see Figure 7c), the maximum amplification factors are absent.

Profile FF' is considered a reverse fault case study (see Figure 8a). In Figure 8b, the maximum amplification factors are limited and existed at 15 m depth for a horizontal

spread along the ground surface from 50 m to 150 m. This could be attributed to the presence of trapped energy in the hanging wall side of these reverse faults at this frequency band width. At a frequency band width of 10 ~ 7 Hz, anomalous maximum amplification factors appear at 15 m depth for a horizontal spread along the ground surface from 300 m to 500 m, as shown in Figure 8c. These anomalous maximum amplification factors could be attributed to the guiding effects of *S*-waves in the same direction of the dipping fault planes of these reverse faults. At a frequency band width of 7 ~ 5 Hz, profile FF' (Figure 8d) exhibits maximum amplification factors along the ground surface. This amplification pattern seems unaffected by the presence of the reverse fault.

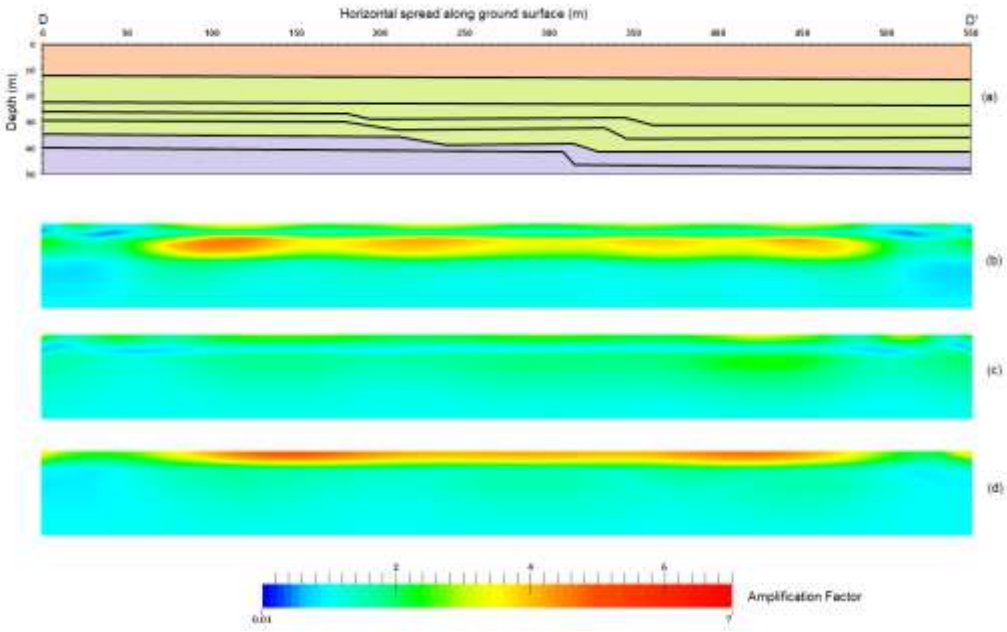

Figure 7. Amplification patterns for profile DD' (a) at frequency bands of 15 ~ 10 Hz (b), 10 ~ 7 Hz (c), and 7 ~ 5 Hz (d).

As shown in Figure 9a and Figure 10a, correspondingly, the CC and EE profiles have been affected by normal and reverse faults. In profile CC', the normal and reverse faults are present only in the bedrock unit. At a frequency band width of 15 ~ 10 Hz, the maximum amplification factors exist at 20 m depth for a horizontal spread along the ground surface between 50 m to 500 m, as shown in Figure 9b. In Figure 9c, the maximum amplification factors are absent at a frequency band width of 10 ~ 7 Hz, whereas a surficial anomalous maximum amplification pattern appears at a frequency band width of 7 ~ 5 Hz, as given in Figure 9d.

In Profile EE' (see Figure 10a), the reverse fault extends at a horizontal spread along the ground surface from 100 m to 375 m, whereas the normal fault extends from

375 m to 500 m. At a frequency band width of 15 ~ 10 Hz, the maximum amplification factors appear only above the normal fault zone at 10 m depth, as given in Figure 10b. At frequency band width of 10 ~ 7 Hz, the maximum amplification factors appear mainly above the reverse fault zone at 15 ~ 20 m depth, as given in Figure 10c. Figure 10d shows the maximum amplification factors that result from the profile EE' at a frequency band width of 7 ~ 5 Hz.

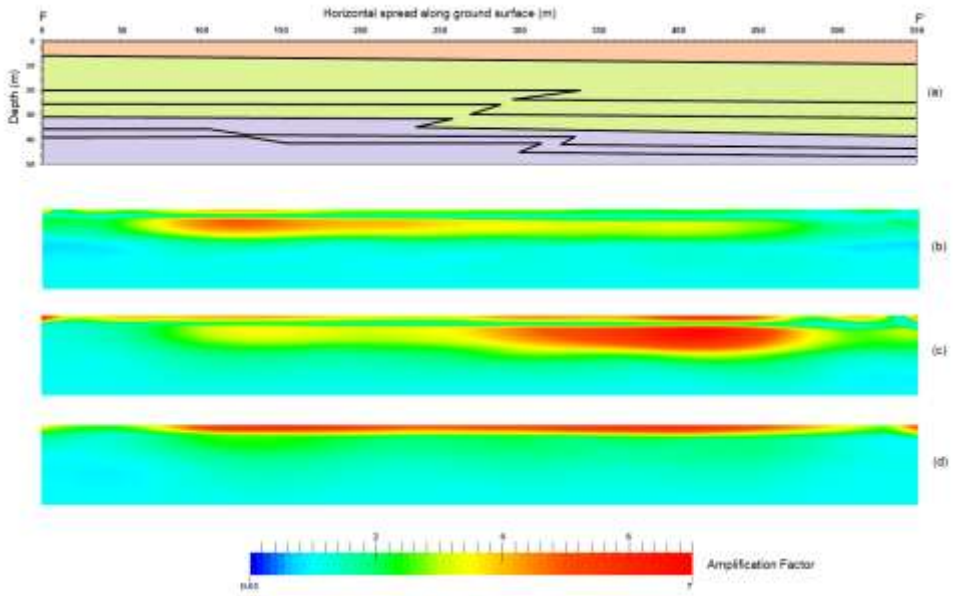

Figure 8. Amplification patterns for profile FF' (a) at frequency bands of 15 ~ 10 Hz (b), 10 ~ 7 Hz (c), and 7 ~ 5 Hz (d).

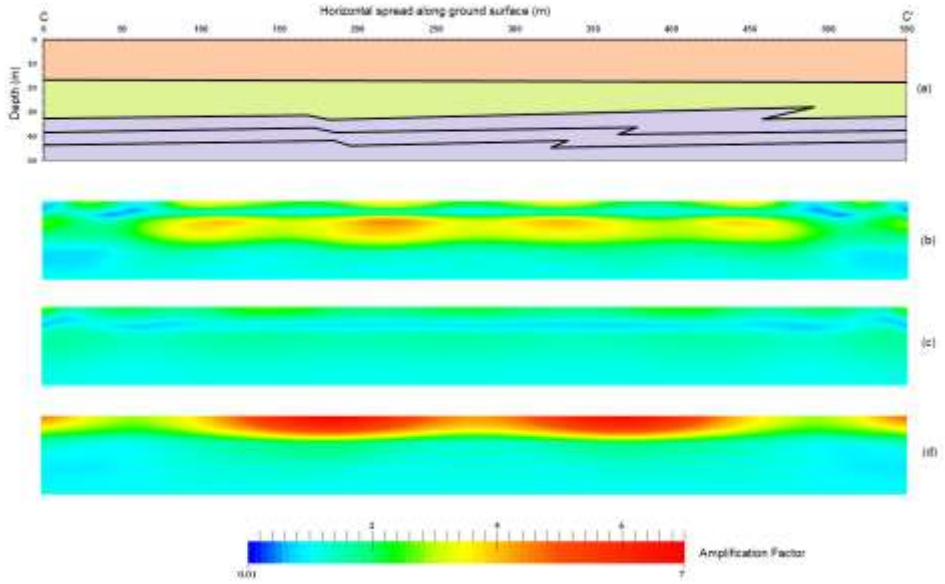

Figure 9. Amplification patterns for profile CC' (a) at frequency bands of 15 ~ 10 Hz (b), 10 ~ 7 Hz (c), and 7 ~ 5 Hz (d).

Normal Fault Profiles AA', BB', and DD' represent normal fault case studies. The presence of the maximum spectral amplification is a trade-off relationship between the frequency and the dip direction of the fault planes. Profile BB' shows an anomalous maximum spectral amplification pattern at a frequency band width of 10 ~ 7 Hz, which could be attributed to the presence of trapped energy in the hanging wall side of this normal fault condition.

Profile FF' represents a reverse fault case study. At a frequency band width of 15 ~ 10 Hz, trapped energy appears in the hanging wall side of these reverse faults. At a frequency band width of 10 ~ 7 Hz, anomalous maximum amplification factors appear because of guiding effects for *S*-waves in the same direction of the dipping fault planes of these reverse faults. This amplification pattern seems uninfluenced by the presence of the reverse fault at a frequency band width of 7 ~ 5 Hz.

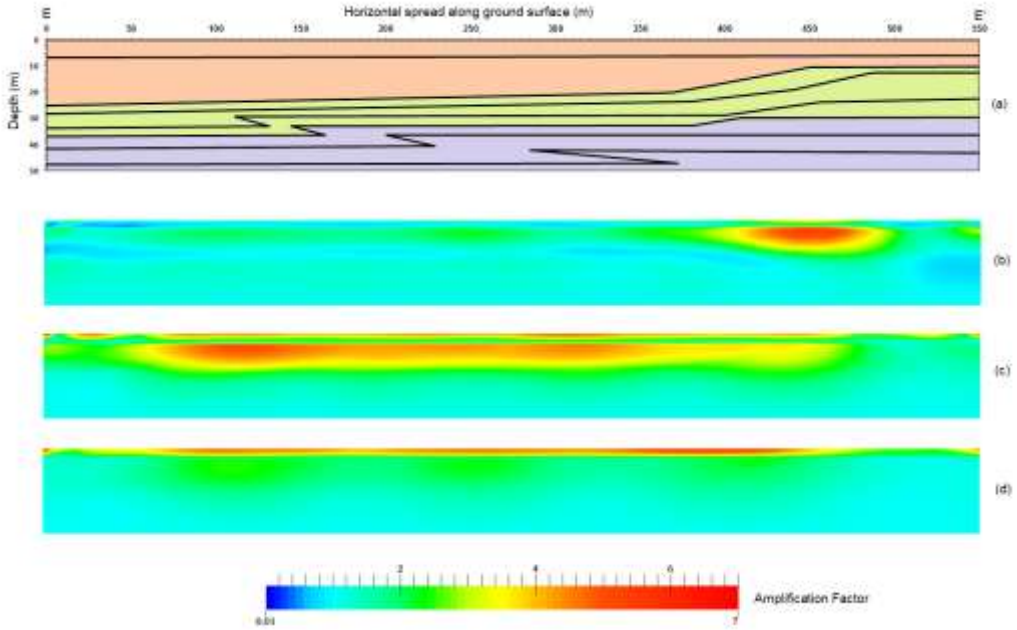

Figure 10. Amplification patterns for profile EE' (a) at frequency bands of 15 ~ 10 Hz (b), 10 ~ 7 Hz (c), and 7 ~ 5 Hz (d).

Profiles CC' and EE' represent normal and reverse faults together. Profile CC' produces modest amplification factors that are distributed at a depth of 20 m and a frequency band width of 15 ~ 10 Hz. This could be attributed to two reasons. Firstly, the normal and reverse faults are present only in the bedrock unit. Consequently, the seismic impedance contrast in the fault zone is absent. Secondly, the gentle dip of the reverse fault plane may cause scattering of the *S*-wave guiding energy along the dip direction of the reverse fault plane. At frequency band widths of 10 ~ 7 Hz and 7 ~ 5 Hz, the amplification patterns indicate that the presence of normal and reverse faults CC' could

not produce enough *S*-waves guiding energy. In Profile EE', the reverse fault amplifies the guided *S*-waves energy at frequency band width of 10 ~ 7 Hz, whereas the normal fault causes maximum amplification factors at a frequency band width of 15 ~ 10 Hz. At a frequency band width of 7 ~ 5 Hz, the resulted amplification pattern seems uninfluenced by presence both of reverse and normal faults.

The fundamental resonance frequencies of the upper layer (*i.e.* alluvial deposits) at the six shallow 2D profiles are comparable to each other because the study area is very limited, yet significant variations in amplification patterns could be achieved among all the profiles. The major role of different fault zone structures in guiding *S*-wave propagation is obvious in these faulted profiles. Studying the spectral amplification patterns for the *S*-waves proves that the *S*-wave's propagation direction is parallel to the dipping direction of the fault plane, whether this fault is a normal fault or a reverse fault. Moreover, the spectral amplification patterns are highly dependent on the frequency band width and on the fault parameters, such as fault zone width, fault plane dip, and fault continuity in layers.

CONCLUSION

In the present study, 2D finite element simulations using equivalent linear analyses have been carried out along six well-defined 2D shallow profiles in Wadi Natash area. Wadi Natash area is in the Eastern Desert of Egypt. At 50 m depth, seismograms with different predominant frequencies were synthesized and used as input ground motions. The analyses gave a good indication of the high influence on local site effects due to the presence of shallow fault zone structures. Studying the amplification patterns from those six shallow 2D profiles clarifies the resultant site effects due to various fault zone structures.

The major role of different fault zone structures in guiding *S*-wave propagation is obvious in these faulted profiles. Studying the spectral amplification patterns for the *S*-waves proves that the *S*-wave's propagation direction is parallel to the dipping direction of the fault plane, whether this fault is a normal fault or a reverse fault. The spectral amplification patterns are highly dependent on the frequency band width and on the fault parameters, such as fault zone width, fault plane dip, and fault continuity in layers.

Ideally, more analyses should be conducted for a range of observed ground motions sufficient to provide significant fault zone-related site response parameters for different locations in Egypt. Also, quantitative relationships for guiding *S*-wave propagation due to different fault zone structures in Wadi Natash will be systematically evaluated. These analyses would be crucial in providing more robust validation for the reliability and potential of dynamic response analyses due to the influence of shallow non-reduced velocity fault zone structures on the local site effects.

ACKNLOWDGMENT

The author deeply acknowledges Prof. Galal El-Habak and Prof. Awad Omran (Geology Dept., Science Faculty, Assiut University, Assiut, Egypt), and Prof. Raafat Fat-Helbary (Aswan Seismological Center) for constructive guidance during preparing the manuscript. The author is highly appreciative and grateful for the invaluable constructive comments and suggestions from the editor and the reviewers.

REFERENCES

[1] Z. Peng, Y. Ben-Zion, Temporal changes of shallow seismic velocity around the Karadere-Duzce Branch of the North Anatolian Fault and strong ground motion, Pure Appl. Geophys., 163(2006), 567-600.

[2] L. Peruzza, R. Azzaro, R. Gee, S. D'Amico, H. Langer, G. Lombardo, B. Pace, M. Pagani, F. Panzera, M. Ordaz, M. L. Suarez, G. Tusa, When probabilistic seismic hazard climbs volcanoes: the Mt. Etna case, Italy – part 2: Computational implementation and first results, Nat. Hazards Earth Syst. Sci., 17(2017), 1999–2015. https://doi.org/10.5194/nhess-17-1999-2017.

[3] G. Tortorici, G. Romagnoli, S. Grassi, S. Imposa, G. Lombardo, F. Panzera, S. Catalano, Quaternary negative tectonic inversion along the Sibillini Mts. Thrust zone: the Arquata del Tronto case history (Central Italy), Environ. Earth Sci., 78-1(2019), 37. https://doi.org/10.1007/s12665-018-8021-2.

[4] P. Spudich, M. Hellweg, H. K. Lee, Directional topographic site response at Tarzana observed in aftershocks of the 1994 North-ridge, California, earthquake: implications for mainshock motions, Bull. Seismol. Soc. Am., 86(1996), S193–S208.

[5] M. Pischiutta, M. K. Savage, R. A. Holt, F. Salvini, Fracture-related wavefield polarization and seismic anisotropy across the Greendale Fault, J. Geophys. Res. Solid Earth, 120(2015), 7048–7067, doi:10.1002/2014JB011560.

[6] F. Panzera, S. D'Amico, E. Colica, M. Viccaro, Ambient vibration measurements to support morphometric analysis of a pyroclastic cone, Bull. Volcanol. 81-12 (2019), 74, https://doi.org/10.1007/s00445-019-1338-1.

[7] F. Panzera, G. Tortorici, G. Romagnoli, G. Marletta, S. Catalano, Empirical evidence of orthogonal relationship between directional site effects and fracture azimuths in an active fault zone: The case of the Mt. Etna lower eastern flank, Engineering Geology, 279(2020), 105900, https://doi.org/10.1016/j.enggeo.2020.105900

[8] M. Pischiutta, M. Fondriest, M. Demurtas, F. Magnoni, G. Di Toro, A. Rovelli, Structural control on the directional amplification of seismic noise (Campo Imperatore, Central Italy), Earth Planet. Sci. Lett., 471(2017), 10–18, https://doi.org/10.1016/j.epsl.2017.04.017.

[9] A. E. El-Haddad, New Approach for SH-wave Generation and its Application in Studying The Subsurface Geologic Section of Wadi Natash Area, Eastern Desert-Egypt, Journal of Applied Geophysics, Egyptian Society of Petrophysics, 7-1(2008), 361-387

[10] H. Fritz, D. R. Dallmeyer, E. Wallbrecher, J. Loizenbauer, G. Hoinkes, P. Neymayr, A. A. Khudeir, Neoproterozoic tectonothermal evolution of the Central Eastern Desert, Egypt: a slow velocity tectonic process of core complex exhumation, Journal of African Earth Sciences, 34(2002), 137–155.

[11] M. M. Abdeen, M. F. Sadek, R. O. Greiling, Thrusting and multiple folding in the Neoproterozoic Pan-African basemenet of Wadi Hodein area, south Eastern Desert, Egypt, Journal of African Earth Sciences, 52(2008), 21–29.

[12] A. Kröner, R. O. Greiling, T. Reischmann, I. M. Hussein, R. J. Stern, S. Durr, J. Kruger, M. Zimmer, Pan-African crustal evolution in the Nubian segment of northeast Africa. In: Kröner, A. (Ed.), Proterozoic Lithospheric Evolution, American Geophysical Union. Geodynamics Series, vol. 17(1987), 237–257.

[13] G. H. F. Gardner, L. W. Gardner, A. R. Gregory, Formation velocity and density – The diagnostic basics for stratigraphic traps, Geophysics, 39(1974), 770-780.

[14] D. M. Boore, SMSIM-Fortran Programs for Simulating Ground Motions from Earthquakes: Version 2.3., U.S. Geological Survey, Open File Report: 96-80-A, (2005)

[15] D. W. Simpson, Personal Communication. Lamont-Doherty Geological Observatory, Palisades, New York 10964, USA, (1984)

[16] B. Niceno, EasyMesh- A Two-Dimensional Quality Mesh Generator: Version 1.4., Trieste University, Italy, (2002)

[17] M. Hudson, I. M. Idriss, M. Beikae, QUAD4M: A Computer Program to Evaluate the Seismic Response of Soil Structures using Finite Element Procedures and Incorporating a Compliant Base, Center for Geotechnical Modeling, Dep. of Civil &Env. Engng, University of California, Davis, USA, (1994)